Measurement-Constrained Sampling for Text-Prompted Blind Face Restoration

Wenjie Li¹, Yulun Zhang², Guangwei Gao³, Heng Guo¹, and Zhanyu Ma¹

¹Beijing University of Posts and Telecommunications

²Shanghai Jiao Tong University ³Nanjing University of Science and Technology

{cswjli, guoheng, mahzhanyu}@bupt.edu.cn, {yulun100, csggao}@gmail.com

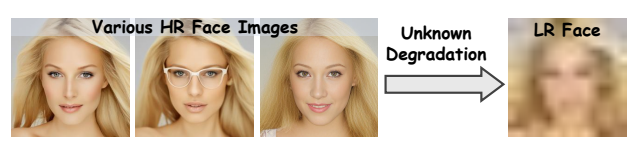
Abstract

Blind face restoration (BFR) may correspond to multiple plausible high-quality (HQ) reconstructions under extremely low-quality (LO) inputs. However, existing methods typically produce deterministic results, struggling to capture this oneto-many nature. In this paper, we propose a Measurement-Constrained Sampling (MCS) approach that enables diverse LQ face reconstructions conditioned on different textual prompts. Specifically, we formulate BFR as a measurementconstrained generative task by constructing an inverse problem through controlled degradations of coarse restorations, which allows posterior-guided sampling within text-to-image diffusion. Measurement constraints include both Forward Measurement, which ensures results align with input structures, and Reverse Measurement, which produces projection spaces, ensuring that the solution can align with various prompts. Experiments show that our MCS can generate prompt-aligned results and outperforms existing BFR methods. Codes will be released after acceptance.

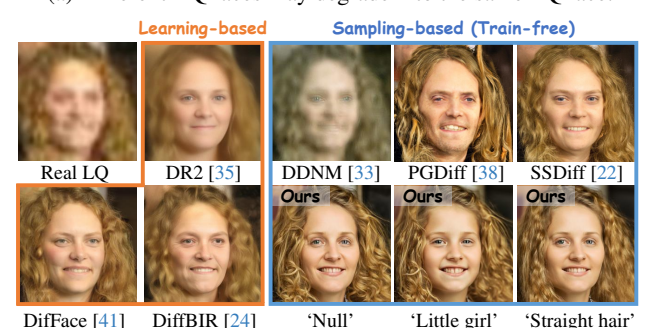
1. Introduction

Blind face restoration (BFR) aims to reconstruct high-quality (HQ) facial images from low-quality (LQ) inputs with unknown and complex degradations, which has been extensively studied in recent years [20]. This task becomes particularly ambiguous under extremely LQ conditions, where a single input may correspond to multiple semantically plausible HR reconstructions [20]. As illustrated in Fig. 1, different face images with varying attributes (*e.g.*, expressions, hairstyles, accessories) may degrade into visually similar LQ observations. Therefore, this one-to-many nature not only increases the challenge of restoration but also reveals the potential for personalized and controllable BFR.

However, existing BFR [24, 32, 35, 38] methods struggle to capture such one-to-many uncertainty in blind degradations, limiting their flexibility in applications. Specifically, with the increasing adoption of diffusion models [15] in BFR, surpassing the performance of GAN-based methods [32, 43],



(a) Different HQ faces may degrade into the same LQ face.



(b) Our method can generate high-quality prompt-aligned faces.

Figure 1. Illustration of the one-to-many nature of blind degradations and the effectiveness of our method in generating diverse, prompt-aligned face images from extremely low-quality inputs.

existing diffusion-based methods can be broadly classified into two categories: *i) Learning-based methods* [24, 35] typically rely on supervised training with paired low- and high-quality data, and are often optimized to produce a single deterministic output, making them inadequate for modeling the inherent one-to-many correspondence under severe degradations. *ii) Sampling-based methods* [6, 22, 33, 38] typically accomplish restoration by modifying the sampling trajectory of pre-trained diffusion models, enabling zero-shot, training-free adaptation to a variety of restoration tasks.

Sampling-based approaches utilizing inverse problem solving [1, 6, 33], though not inherently text-driven, show potential for generating diverse outputs when combined with pre-trained text-to-image (T2I) diffusion models. Specifically, these methods define a degradation operation A, guiding each step \hat{x}_t of the reverse diffusion to degenerate to LQ inputs I_{LQ} , e.g., A (\hat{x}_t) $\rightarrow I_{LQ}$. Since HQ faces with varying attributes may map to the same LQ face, this approach, when integrated with text guidance, can produce a solution space with various HQ faces exhibiting diverse attributes. However,

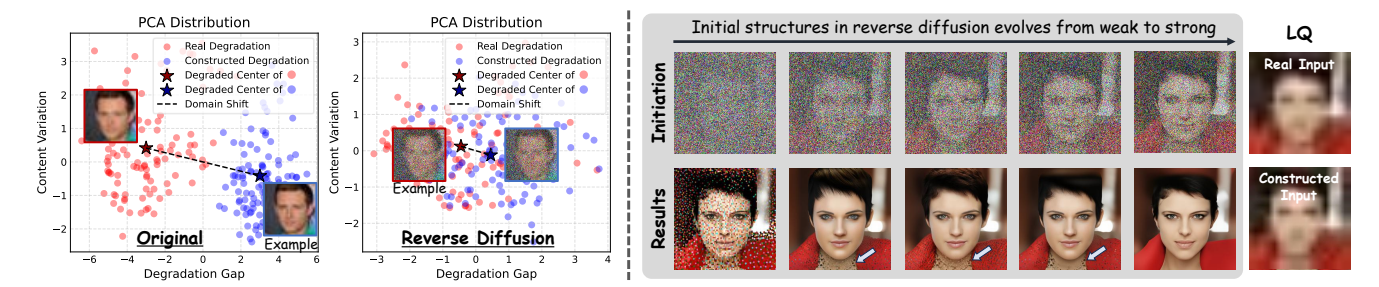


Figure 2. (**Left**) While real and constructed degradations differ, the gap diminishes in reverse diffusion, making constructed observations suitable anchors of inverse problem solving for guided sampling. (**Right**) When facial structures in noisy samples are unclear in the reverse diffusion process of T2I diffusion, inverse problem solving centred on constructed degradations amplifies noise, resulting in artifacts.

its applicability is limited, as it often assumes prior knowledge of the degradation operation A, which is challenging to satisfy in blind or real-world degradation contexts.

Building on the successes and limitations mentioned above, we aim to construct a degradation observation that approximates real degradation in the T2I diffusion while enabling the solution of inverse problems. Therefore, we explore the relationship between real degradation and constructed degradation (e.g., bicubic interpolation applied to results after a restoration process input). As shown in the left panel of Fig. 2, during the reverse diffusion process, where noise dominates, the gap between constructed and real degradation significantly narrows. This observation led us to formulate an inverse problem in which constructed degradation can serve as an anchor for reverse diffusion. However, as shown in the right panel of Fig. 2, this formulation can disrupt the reverse diffusion process when facial structures in noisy samples are unclear, resulting in pronounced artifacts. The solution of the inverse problem can be mitigated when facial structures in the noisy samples are well-defined.

Based on these observations, we propose a Measurement-Constrained Sampling (MCS) that unifies text-driven control and measurement guidance within pre-trained T2I diffusion. To solve the inverse problem, we first apply a constructed degradation to the rough estimate from the restorer [4], creating an anchor. Simultaneously, we introduce a Reverse Measurement to constrain the denoising trajectory within a degradation-consistent projection space, anchored by the constructed degradation and guided by prompts. To avoid artifacts arising from the reverse strategy when facial structures are unclear in denoised samples, as discussed in Sec. 4.1, we introduce a Forward Measurement in early sampling steps to approximate restoration that aligns with the structures of inputs. Additionally, we employ noise-blended anchors to initialize reverse diffusion, providing an approximate facial structure and bridging the domain gap between synthesis and real degradation under noise dominance.

To the best of our knowledge, our MCS is the first BFR method capable of generating text-prompt-aligned faces in a training-free manner. As shown in Fig. 1, benefiting from

balancing Forward and Reverse Measurement, our MCS outperforms existing learning-based [24, 35, 41] and sampling-based [22, 33, 38] diffusion methods in both BFR diversity and quality. In summary, our contributions are as follows:

- We leverage pre-trained T2I models to reconstruct diverse HR faces from blind LR inputs, guided by both text-based semantics and measurement consistency constraints;
- We introduce forward measurements to approximate degradations like facial structures, and reverse measurements to expand generative spaces for satisfying diversity prompts;
- Under blind degradation, our MCS produces accurate face results without prompts and generates text-aligned faces when guided, outperforming existing BFR methods.

2. Related Work

2.1. Blind Face Restoration

To avoid the limitations of non-blind methods [5, 21, 29, 37], which are difficult to generalize to realistic degradations, blind FSR has seen rapid progress in recent years. Early approaches [23, 34] enhanced networks by incorporating face dictionary priors, but these methods lack robustness under extremely LR conditions. To address this, recent works incorporate generative priors into networks. Specifically, GLEAN [2], GPEN [40], GFPGAN [32], and SGPN [44] integrate StyleGAN-based priors into network architectures to boost performance in specific scenarios. VQFR [13], Code-Former [43], and DAEFR [28] further enhance the determinism of facial feature representations by introducing discretized GAN priors, such as pre-trained codebooks, thereby reducing the likelihood of facial artifacts. With the advent of generative diffusion [25] in generative tasks, methods like StableSR [30], DiffBIR [24], OSEDiff [36], and OSD-Face [31] improve FSR by training lightweight controllable models to harness the generative diffusion prior. However, these methods require large-scale paired data training and can produce only a single deterministic restoration result.

2.2. Guided Sampling-based Diffusion

Recent efforts have focused on developing efficient samplingguided strategies for pre-trained diffusion models to enable

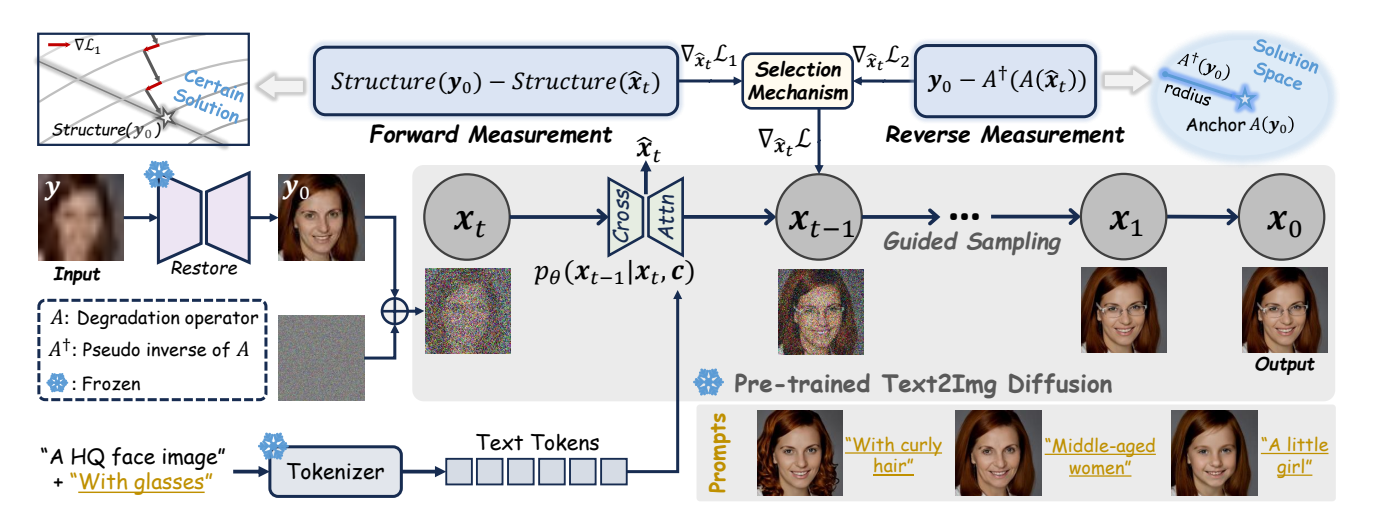


Figure 3. Our method utilizes *Forward Measurement* to align solutions with input structures, where structural components after the wavelet decomposition define the structure. *Reverse Measurement* ensures solutions lie within the degenerate space centered on anchor points. Therefore, under the guidance of texts, our method can generate diverse facial results that satisfy both degeneracy and textual constraints.

zero-shot image restoration without training. Early methods such as DDRM [17], IIGDM [27], DDNM [33], FPS [10], and MCGDiff [1] rely on known linear degradation models (e.g., bicubic downsampling) and their corresponding inverses to guide the restoration process. Later approaches, including DPS [6] and GDP [11], replace explicit likelihood modeling with hard data consistency constraints to tackle more complex nonlinear degradation, enabling approximate posterior inference during denoising. Gandikota et al. [12] further explore text-guided restoration using these sampling frameworks to benchmark performance. However, the above methods assume simple degradation and struggle in blind degradation settings. PGDiff [38] addresses this by leveraging high-quality attribute guidance. Furthermore, SSDiff [22] guides the sampling process by constructing high-quality pseudo labels for degradation faces. However, the resulting restorations are deterministic and lack diversity. In contrast, our method handles blind degradation while generating diverse, text-aligned outputs through guided sampling.

3. Preliminaries

3.1. Diffusion Models

The diffusion generative model [15] is designed to approximate the data distribution $q(x_0)$. It consists of two stages:

The Forward Diffusion process defined as a Markov chain of step length T, where Gaussian noise is incrementally added to the data x_0 using a fixed noise schedule $\beta_1, ..., \beta_T$, progressively corrupting the original input:

$$q(\boldsymbol{x}_{t}|\boldsymbol{x}_{t-1}) = \mathcal{N}\left(\boldsymbol{x}_{t}; \sqrt{1-\beta_{t}}\boldsymbol{x}_{t-1}, \beta_{t}\boldsymbol{I}\right).$$
(1)

The forward noise processing can be sampled directly from

 x_0 to any step x_t by the following equation:

$$x_t = \sqrt{\overline{\alpha}_t} x_0 + \sqrt{1 - \overline{\alpha}_t} \epsilon, \quad \epsilon \sim \mathcal{N}(0, \mathbf{I}),$$
 (2)

where
$$\alpha_t = 1 - \beta_t$$
 and $\overline{\alpha}_t = \prod_{i=0}^t \alpha_i$.

The Reverse Diffusion process iteratively reconstructs clean data x_0 starting from the Gaussian noise distribution $x_T \sim \mathcal{N}(0, I)$, following a Markov chain [15] structure with Gaussian transitions:

$$p_{\theta}\left(\boldsymbol{x}_{t-1}|\boldsymbol{x}_{t}\right) = \mathcal{N}\left(\boldsymbol{x}_{t-1};\boldsymbol{\mu}_{\theta}\left(\boldsymbol{x}_{t},t\right), \boldsymbol{\Sigma}_{\theta}(\boldsymbol{x}_{t},t)\right), \quad (3)$$

where $\Sigma_{\theta}(\boldsymbol{x}_t,t) = \frac{1-\overline{\alpha}_{t-1}}{1-\overline{\alpha}_t}\beta_t \boldsymbol{I}$, $\boldsymbol{\mu}_{\theta}\left(\boldsymbol{x}_t,t\right)$ is the mean value we estimate by a deep network $\boldsymbol{\epsilon}_{\theta}$ from \boldsymbol{x}_t as follows:

$$\boldsymbol{\mu}_{\theta}\left(\boldsymbol{x}_{t},t\right) = \frac{1}{\sqrt{\alpha_{t}}} \left(\boldsymbol{x}_{t} - \frac{\beta_{t}}{\sqrt{1 - \overline{\alpha}_{t}}} \boldsymbol{\epsilon}_{\theta}\left(\boldsymbol{x}_{t},t\right)\right). \tag{4}$$

In practice, we can directly approximate \hat{x}_0 from x_t :

$$\hat{\boldsymbol{x}}_0 = \boldsymbol{x}_t / \sqrt{\bar{\alpha}_t} - \boldsymbol{\epsilon}_{\theta}(\boldsymbol{x}_t, t) \sqrt{(1 - \bar{\alpha}_t) / \bar{\alpha}_t}. \tag{5}$$

3.2. Inverse Problem Solving With Diffusion Model

In practice [17], the full data x_0 is unavailable; instead, we observe a degraded measurement y through $y = A(x_0) + n$, where $A(\cdot)$ denotes the measurement operator and n is observation noise (e.g., Gaussian noise).

Diffusion models serve as priors over $p(x_0)$, allowing approximate posterior sampling from $p(x_0|y)$ via a modified reverse process. To incorporate measurements into the unconditional diffusion framework, we inject a data-consistency gradient at each step, approximating the likelihood term as:

$$\nabla_{\boldsymbol{x}_t} \log p(\boldsymbol{y} \mid \boldsymbol{x}_t) \approx -\lambda \cdot \nabla_{\boldsymbol{x}_t} \|\boldsymbol{y} - A(\hat{\boldsymbol{x}}_0)\|^2, \quad (6)$$

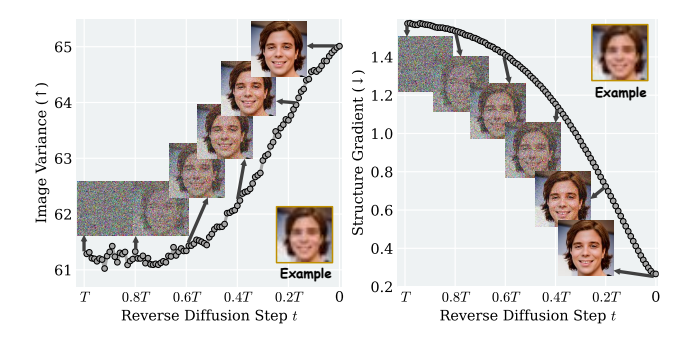


Figure 4. We perform a statistical analysis of the pre-trained T2I [26] model's convergence during reverse diffusion on CelebA-HQ test set. Image variance, structural gradients, and selected visualizations all show that the T2I model first reconstructs structural features in a small portion of facial regions, then refines the detailed features covering the majority of facial regions.

where \hat{x}_0 is an estimate of clean datas derived from x_t using Eq. (5). This correction modifies the predicted mean $\tilde{\mu}_{\theta}$:

$$\tilde{\boldsymbol{\mu}}_{\theta}(\boldsymbol{x}_{t}, t, \boldsymbol{y}) = \boldsymbol{\mu}_{\theta}(\boldsymbol{x}_{t}, t) - \lambda \cdot \nabla_{\boldsymbol{x}_{t}} \|\boldsymbol{y} - A(\hat{\boldsymbol{x}}_{0})\|^{2}, \quad (7)$$

used during the posterior-guided reverse sampling step:

$$\boldsymbol{x}_{t-1} \sim \mathcal{N}\left(\tilde{\boldsymbol{\mu}}_{\theta}(\boldsymbol{x}_t, t, \boldsymbol{y}), \Sigma_{\theta} \mathbf{I}\right).$$
 (8)

By injecting gradients $\nabla_{x_t} \log p(y \mid x_t)$ into the reverse diffusion steps, inverse problem solving can be performed as approximate posterior sampling [6].

4. Method

As shown in Fig. 3, for an extremely blurred facial input y and a given textual prompt c, our goal is to ensure that restored facial results x_0 satisfy both input degradations and prompt conditions. To this end, we reformulate BFR as a balance between degradation consistency and diversity, with degradation consistency enforced by Forward Measurements and diversity achieved through text-guided alignment in inverse projection spaces derived from degradation-aligned sampling. To ensure that Reverse Measurements are applied only after structural features have stabilized, we introduce a Selection Mechanism that determines when each measurement operates. Algorithm 1 summarizes the guided sampling process of our MCS. The following sections detail our guided sampling process, including Forward Measurement, Reverse Measurement, and Selection Mechanism.

4.1. Selection Mechanism.

Before introducing forward and reverse measurements, we first outline the selection mechanism for these approaches at different stages of reverse diffusion. As discussed in Fig. 2, inverse problem solving is applied during reverse diffusion to expand the solution space and integrate text guidance

Algorithm 1 Sampling process of our MCS.

Input: Extremely LQ face \boldsymbol{y} , text tokens \boldsymbol{c} . Require: Pre-trained T2I $(\mu_{\theta}(\boldsymbol{x}_t,t), \Sigma_{\theta}(\boldsymbol{x}_t,t))$ and Restore \mathcal{R} , Degradation A and its pseudo inverse A^{\dagger} . Output: Text-aligned HQ face \boldsymbol{x}_0 . $\boldsymbol{x}_t = \sqrt{\bar{\alpha}_t} \cdot \mathcal{R}(\boldsymbol{y}) + \sqrt{1 - \bar{\alpha}_t} \cdot \boldsymbol{\epsilon}, \quad \boldsymbol{\epsilon} \sim \mathcal{N}(0,\mathbf{I})$ for t from T to 1 do $\hat{\boldsymbol{x}}_t \leftarrow \frac{1}{\sqrt{\bar{\alpha}_t}} \boldsymbol{x}_t - \sqrt{\frac{1 - \bar{\alpha}_t}{\bar{\alpha}_t}} \boldsymbol{\epsilon}_{\theta}(\boldsymbol{x}_t,t,\boldsymbol{c})$ if t in Selection then $\boldsymbol{x}_{t-1} \sim \boldsymbol{x}_t - \nabla_{\hat{\boldsymbol{x}}_t} \|\mathcal{R}(\boldsymbol{y})|_{Struct} - \hat{\boldsymbol{x}}_t|_{Struct}\|_2^2$ else $\boldsymbol{x}_{t-1} \sim \boldsymbol{x}_t - \nabla_{\hat{\boldsymbol{x}}_t} \|\mathcal{R}(\boldsymbol{y}) - A^{\dagger} (A(\hat{\boldsymbol{x}}_t))\|_2^2$ end if $\boldsymbol{x}_{t-1} \sim \mathcal{N}(\mu_{\theta}(\boldsymbol{x}_t,t) - \Sigma_{\theta}(\boldsymbol{x}_t,t)\nabla\mathcal{L}, \Sigma_{\theta}(\boldsymbol{x}_t,t))$ end for return \boldsymbol{x}_0

once facial structures stabilize. Figure 4 presents the convergence trends of pre-trained T2I diffusion models, indicating that reverse diffusion initially focuses on facial structure before gradually refining details. Based on this observation, we apply forward measurement during the initial phase [T,0.6T] to guide facial structure adaptation to degenerate inputs. Once facial structure stabilizes, reverse measurement is introduced during the interval [0.6T,0], progressively incorporating text alignment constraints to ensure the solution space accommodates varying textual conditions. This coarse-to-fine design ensures that generated images conform to degraded face structures and textual measurements.

4.2. Forward Measurement.

As shown in Fig. 3, forward measurement is formulated as a joint guidance of textual prompts and coarse HR estimates. First, let p denote a user-specified textual prompt (e.g., "a woman with glasses"), which is embedded by a pretrained text tokenizer $\varepsilon_{\text{text}}$ in the T2I Diffusion model [26] to produce contextual features $c = \varepsilon_{\text{text}}(p)$. These embeddings are injected into each denoising step of the UNet backbone within the diffusion model, thereby conditioning the predicted posterior distribution:

$$p_{\theta}(\boldsymbol{x}_{t-1} \mid \boldsymbol{x}_{t}, \boldsymbol{c}) = \mathcal{N}(\boldsymbol{\mu}_{\theta}(\boldsymbol{x}_{t}, t, \boldsymbol{c}), \boldsymbol{\Sigma}_{\theta} \mathbf{I}), \tag{9}$$

where μ_{θ} is the model-predicted mean conditioned on the noisy input x_t and prompt embedding c, guiding the generative trajectory toward the target semantics. However, relying solely on textual constraints often fails to produce results closely aligned with the desired output.

To incorporate semantic constraints, we initialize the sampling at timestep t with a coarse face estimate y_0 obtained from a pretrained restorer [40], and perturb it with Gaussian

Table 1. Quantitative comparisons on the synthetic CelebA-HQ [16] dataset. **Bold** and <u>underline</u> indicates the best and the second best performance. "L" and "S" represent "Learning-based (Paired-data Training)" and "Sampling-based (Zero-shot, Train-free)". For this Table and Table 2, our method is evaluated under the prompt-free setting (*i.e.*, prompts are set to empty).

	Туре	×16			×8			×4					
Methods		MUSIQ↑	MAN-IQA↑	DISTS↓	LPIPS↓	MUSIQ↑	MAN-IQA↑	DISTS↓	LPIPS↓	MUSIQ↑	MAN-IQA↑	DISTS↓	LPIPS↓
DR2 [35]	L	27.05	0.2225	0.3210	0.4785	31.72	0.2483	0.2899	0.4224	21.81	0.1696	0.3280	0.4701
DifFace [41]	L	37.77	0.2042	0.2657	0.3824	54.51	0.2870	0.2239	0.2966	61.38	0.3574	0.1955	0.2431
DiffBIR [24]	L	60.45	0.3893	0.2104	0.2856	61.98	0.3926	0.1957	0.2489	61.00	0.3808	0.1855	0.2302
DPS [6]	S	54.36	0.3896	0.3171	0.4917	41.74	0.3515	0.3416	0.4973	26.51	0.1856	0.3249	0.5058
IIGDM [27]	S	49.89	0.3375	0.3283	0.5037	37.88	0.3002	0.3624	0.5328	28.79	0.2828	0.3916	0.5630
DDNM [33]	S	29.30	0.1994	0.3817	0.4479	24.23	0.2091	0.3370	0.5010	29.29	0.2372	0.3133	0.4479
PGDiff [38]	S	55.36	0.3620	0.2193	0.3231	57.27	0.3717	0.2043	0.2784	56.18	0.3771	0.1986	0.2644
MCG-Diff [1]	S	45.28	0.3497	0.3466	0.4734	38.45	0.3342	0.3359	0.4972	27.89	0.2431	0.3298	0.5163
SSDiff [22]	S	61.05	0.3753	0.2228	0.3129	62.22	0.3771	0.2021	0.2713	63.88	0.3750	0.1882	0.2459
Ours	S	62.72	0.4483	0.2215	0.3115	63.02	0.4436	0.1983	0.2649	64.82	0.4632	0.1851	0.2361

Table 2. Quantitative comparisons on real-world datasets [32, 43]. **Bold** and <u>underline</u> indicates the best and the second best results. "L" and "S" represent "Learning-based (Paired-data Training)" and "Sampling-based (Zero-shot, Train-free)".

Methods	Туре	Wider	-Test [43]	WebPhoto-Test [32]		
Wicthous	Type	MUSIQ↑	MAN-IQA↑	MUSIQ↑	MAN-IQA↑	
DR2 [35]	L	39.27	0.2602	32.27	0.2632	
DifFace [41]	L	60.38	0.3516	59.50	0.3365	
DiffBIR [24]	L	62.57	0.3613	65.62	0.4009	
DPS [6]	S	23.28	0.1571	21.22	0.2632	
IIGDM [27]	S	22.67	0.1557	42.91	0.2831	
DDNM [33]	S	22.80	0.1959	22.13	0.1485	
PGDiff [38]	S	61.28	0.3496	61.75	0.3655	
MCG-Diff [1]	S	23.34	0.1533	20.57	0.2493	
SSDiff [22]	S	62.44	0.3669	66.17	0.4002	
Ours	S	68.08	0.4236	69.74	0.4652	

noise to align with the diffusion distribution:

$$x_t = \sqrt{\bar{\alpha}_t} \cdot y_0 + \sqrt{1 - \bar{\alpha}_t} \cdot \epsilon, \quad \epsilon \sim \mathcal{N}(0, \mathbf{I}).$$
 (10)

Unlike previous works [24, 35] that initialize from pure noise, we ensure that early samples are structurally consistent with high-quality attribute observation [22, 38]. Specifically, at each denoising step, denoise models predict a clean signal $\hat{x}_t = \mu_{\theta}(x_t, t, c)$, conditioned on prompt semantics. To preserve consistency with the proxy y_0 , we first apply Haar wavelet decomposition \mathcal{WD} , thereby obtaining a combination comprising a high-frequency portion VHD formed by merging three high-frequency subbands and a low-frequency subband portion L. To facilitate the convergence of structures in intermediate states, we select high-frequency portion that primarily reflect facial structure:

$$\left\{\boldsymbol{y}_{L}^{0},\boldsymbol{y}_{V\!H\!D}^{0}\right\},\left\{\hat{\boldsymbol{x}}_{L}^{t},\hat{\boldsymbol{x}}_{V\!H\!D}^{t}\right\}\!=\!\mathcal{W}\mathcal{D}\left(\boldsymbol{y}_{0}\right),\mathcal{W}\mathcal{D}\left(\hat{\boldsymbol{x}}_{t}\right).\tag{11}$$

Then we impose a forward measurement loss:

$$\mathcal{L}_1 = \left\| \boldsymbol{y}_{VHD}^0 - \hat{\boldsymbol{x}}_{VHD}^t \right\|_2^2, \tag{12}$$

Meanwhile, the prompt embedding c affects the gradient through \hat{x}_t , allowing semantic cues (e.g., "with glasses") to influence the direction and content of the update.

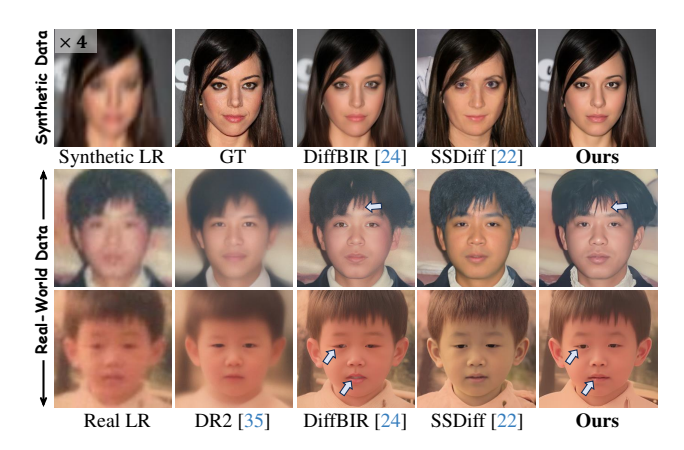


Figure 5. Quantitative results under mild degradation without textual prompts. Our method can achieve higher BFR quality than the latest learning-based [24, 35] and sampling-based [22] methods.

Finally, the next intermediate step x_{t-1} is refined through a gradient-guided sampling scheme [7]:

$$x_{t-1} \leftarrow \sqrt{\bar{\alpha}_t} \cdot y_0 + \sqrt{1 - \bar{\alpha}_t} \cdot \epsilon - \eta \nabla_{x_t} \mathcal{L}_1 + \sigma_t \cdot \epsilon,$$
 (13)

where η is a step size hyperparameter. This update encourages the generation to remain faithful to facial measurement structure, ensuring that input degenerate attributes (*e.g.*, overall facial structures of inputs) manifest coherently in outputs.

4.3. Reverse Measurement.

Despite the inclusion of textual prompts in the forward measurement, due to the deterministic nature of forward measurements, overly strong constraints may suppress the diversity of samples aligned with textual prompts. To balance measurement fidelity and semantic expressiveness, as shown in Fig. 3, we introduce an inverse measurement constraint. This constraint encourages generated contents to align with degraded inputs while expanding the potential generative space. Centered on the constructed anchor $A(\boldsymbol{y}_0)$ with a pseudo-inverse range A^\dagger as its radius, this expansion ensures that results remain consistent with the given textual prompt.

Table 3. Comparison on face landmark distance (LMD) (\downarrow) to evaluate fidelity on $\times 8$ CelebA-HQ. Following previous works [22, 31], we don't employ PSNR/SSIM to evaluate fidelity, as these metrics primarily reflect pixel consistency rather than facial identity preservation.

]	Input	DR2 [35]	DifFace [41] DiffBIR	[24] DPS [6] IIGDM [2	27] DDNM [33] PGDiff	[38] MCC	3-Diff [1]	SSDiff [22]	Ours
1	180.4	3.165	2.874	2.05	5.400	6.791	3.010	3.03	1 5	5.742	2.413	2.268
c Data				2					Ours	Ours	Ours	
Je T	Syntr	netic LR	GT	DR2 [35]	DDNM [33]	PGDiff [38]	MCG-Diff [1]	SSDiff [22]	"Null"		r face" "Asian-	looking
* Synthetic	Ñ	netic LR	GT	DR2 [35]	DDNM [33]	PGDiff [38]	MCG-Diff [1]	SSDiff [22]	Ours "Null"	Ours "Little	Ours girl" "Middl	le-aged"
orld Data			DR2 [35]	DiffBIR [24]	DDNM [33]	PGDiff [38]	MCG-Diff [1]	SSDiff [22]	Ours "Null"	Ours "Curly	Ours	nild"
A Real-world	N	al LR	DR2 [35]	DiffBIR [24]	DDNM [33]	PGDiff [38]	MCG-Diff [1]	SSDiff [22]	Ours "Null"	Ours Curs Curs Curs Curs Curs Curs Curs C	Ours	earrings"

Figure 6. Our method maintains high-fidelity restoration under extremely LR conditions, producing visually coherent results when prompts are not provided. Furthermore, our method can achieve accurate semantic alignment when guided by text prompts.

Specifically, we define a known degradation operator A (e.g., average pooling) that maps the coarse HR estimate face \mathbf{y}_0 to the observation anchor $A(\mathbf{y}_0)$, and solve its pseudoinverse A^\dagger using the Singular Value Decomposition (SVD) following [17, 19], which approximates the inverse mapping. At each denoising step, similar to operators in Forward Measurement, we first obtain the predicted clean signal $\hat{x}_t = \mu_{\theta}(\mathbf{x}_t, t, \mathbf{c})$. Then we solve the inverse problem on \hat{x}_t to encourage alignment with the degraded observation:

$$\mathcal{L}_2 = \left\| \boldsymbol{y}_0 - A^{\dagger} \left(A(\hat{\boldsymbol{x}}_t) \right) \right\|_2^2. \tag{14}$$

This measurement is centered on the anchor $A(\boldsymbol{y}_0)$. Geometrically, the reverse measurement constrains $\hat{\boldsymbol{x}}_t$ within the solution space and centres the space on the degenerate anchor point $A(\boldsymbol{y}_0)$. The pseudo-inverse projection via A^\dagger steers the reconstruction toward a solution similar to \boldsymbol{y}_0 . As the state of $\hat{\boldsymbol{x}}_t$ fluctuates at each step during reverse diffusion, AA^\dagger enables the generation of a solution space, which is then guided towards consistent solutions through prompts.

Compared to minimizing $||A(y_0) - A(\hat{x}_t)||_2^2$ [6], which enforces a more strict match in observation spaces, our formulation with $A^{\dagger}A$ introduces a relaxed constraint, allowing for greater diversity. Then, x_{t-1} is refined through gradient-guided sampling. The process is as follows:

$$\boldsymbol{x}_{t-1} \leftarrow \sqrt{\bar{\alpha}_t} \cdot \boldsymbol{y}_0 + \sqrt{1 - \bar{\alpha}_t} \cdot \boldsymbol{\epsilon} - \eta \nabla_{\boldsymbol{x}_t} \mathcal{L}_2 + \sigma_t \cdot \boldsymbol{\epsilon}.$$
 (15)

where η is a step size hyperparameter. This update mechanism encourages the generation to adhere faithfully to given textual conditions (*e.g.*, "a woman with glasses").

Overall, by staged selection optimization of gradient-based loss \mathcal{L}_1 and \mathcal{L}_2 , the T2I diffusion achieves a trade-off between degenerate measurement consistency and textual measurement consistency, enabling generated content to both reflect textual descriptions and satisfy degenerate inputs.

5. Experiments

5.1. Datasets

Our method is training-free and does not require any training dataset. For the synthetic test set, we follow previous BFR methods [2, 3, 14] by selecting 1000 HQ face images from CelebA-HQ [16], resizing these images to the size of 256^2 [9, 27, 33] as ground truth I_{GT} . Following the established protocol [32], we synthesize the corresponding LQ images I_{LQ} using the degradation model described below:

$$I_{LQ} = [(I_{GT} \circledast k_{\sigma}) \downarrow_{s} + n_{\delta}]_{JPEG_{\sigma}}.$$
 (16)

For the Gaussian blur kernel k_{σ} , downsampling operation with a scale factor s (s = 8,16,32), Gaussian noise n_{δ} , and JPEG compressing with quality factor q, we randomly sample σ , δ , q from $\{0.2:10\}$, $\{0:15\}$, $\{60:100\}$, respectively. For real-world test sets, we utilize two widely-used



Figure 7. Ablation studies on our forward measurement (\mathcal{L}_1), where "Pixels" denotes per-pixel gradient-based descent rather than facial structure-based descent like ours.

real-world face benchmarks with degradation levels ranging from heavy to medium: Wider-Test (970 images) [43] and Webphoto-Test (407 images) [32].

5.2. Implementations

For pre-trained Text2Image diffusion models, we use the open-source version of Imagen Deep-Floyd IF [26]. The total number of iteration steps is defaulted to 150. Previous methods, including DifFace [41], DiffBIR [24], PGDiff [38], and SSDiff [22], are implemented at a resolution of 512^2 . However, due to the resolution limitations of the pretrained diffusion model [26] used in our approach, following the strategy of previous pre-trained diffusion-based methods [1, 9, 27, 33], we use official pre-trained weights of 512^2 resolution-based methods to infer outputs and resize these from 512^2 to 256^2 to ensure a fair comparison. As for assessment metrics, we utilize referenced metrics, including DISTS [8], LPIPS [42], and LMD [13]. PSNR and SSIM are not used as they primarily measure pixel similarity rather than face structural similarity. Non-referenced metrics, including MUSIQ [18] and MAN-IQA [39]. The degradation observation radius A for synthetic data is consistent with the super-resolution scale. For real data, we uniformly set the observation radius to 8. All experiments are conducted with PyTorch on an NVIDIA GeForce RTX 4090.

Comparison with Existing Methods We compare our method with two types of existing diffusion-based BFR methods, including: i) Learning-based methods that need paired-data training, including DR2 [35], DifFace [41], and DiffBIR [24]. ii) Sampling-based methods that are zero-shot and train-free, including DPS [6], IIGDM [27], DDNM [33], PGDiff [38], MCG-Diff [1], and SSDiff [22].

Quantitative Comparison. In Table 1 and Table 2, we report results on synthetic [16] and real test sets [32, 43]. Our method achieves the best performance across all noreference metrics, demonstrating its superiority in generating visually high-quality face images. For full-reference metrics, our approach is only surpassed by DiffBIR [24] in a subset of metrics, further indicating competitiveness. Furthermore, in TABLE. 3, following previous works [22, 31], we report face

Table 4. Ablation on text response rate (Reply) and the quality of reconstructed faces (MUSIQ) on ×8 CelebA-HQ, where DDNM [33], DPS [6], and IIGDM [27] are under known degradation.

Method	w/o \mathcal{L}_2	DPS [6]	DDNM [33]	IIGDM [27]	Ours
Reply ↑	41%	32%	88%	36%	91%
MUSIQ ↑	53.4	50.1	22.1	52.2	63.0

Table 5. Ablation on $\mathcal{L}_1/\mathcal{L}_2$ Weight Ratio: balance on text response rate (Reply) and face quality (MUSIQ).

Weight Ratio	2/1	1.5/1	1/1 (Ours)	1/1.5	1/2
Reply ↑	64%	78%	91%	93%	93%
MUSIQ ↑	59.5	59.2	63.0	57.5	53.3

landmark distance (LMD) on CelebA-HQ (\times 8) to measure face fidelity; our method is second only to DiffBIR [24]. These results fully demonstrate that our MCS achieves an excellent balance between restoration fidelity and quality.

Qualitative Comparison. As shown in Fig. 5, we present visual results on synthetic data of $\times 4$ scale and real-world data under mild degradation. On synthetic data, our results are perceptually closer to GT, while on real data, our method restores realistic facial details. Since mild degradation lacks strong one-to-many ambiguity, text-guided results are omitted. In Fig. 6, we evaluate on synthetic data with severe degradations (e.g., $\times 8$ and $\times 16$) and real data. Our method consistently recovers GT-aligned faces on synthetic data and produces natural faces on real data. Moreover, our method effectively incorporates textual prompts, producing results that are not only visually coherent but also aligned with texts, covering attributes such as facial features, age, and accessories, showing the potential of our framework. *More poses of LQ faces can be seen in the supplementary*.

5.3. Ablation Studies

Effectiveness of Forward Measurement. As shown in Fig. 7, we show the effectiveness of our forward measurement. By injecting guidance from a coarse restore estimate, it mitigates early-stage uncertainty and artifacts caused by noise-dominated predictions. In addition, it constrains the inverse measurement process by suppressing excessive uncertainty that may deviate from the true solution. Compared to per-pixel gradient-based descent, it also improves the perceptual quality, as reflected by metrics such as MUSIQ.

Effectiveness of Reverse Measurement. As shown in Table 4, removing our reverse measurement leads to a noticeable drop in response rate. Additionally, compared to methods like DPS and IIGDM, which rely on posterior gradient corrections even under known degradations, their results may suffer from semantic drift due to noise interference, leading to a decrease in response rate. Although DDNM directly projects intermediate samples onto degradation manifolds, leading to high prompt response rates, this approach may

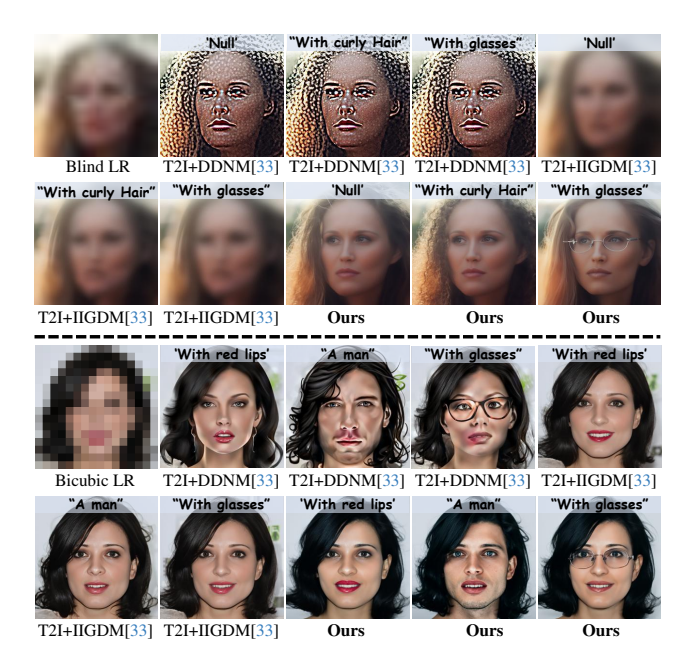


Figure 8. (**Top**): Although sampling strategies like DDNM [33] and IIGDM [27] have the potential to be combined with T2I model [26] for text-aligned reconstruction, their dependence on known degradation limits performance under blind settings. (**Bottom**): Even with known degradation, existing strategies [27, 33] combined with T2I [26] still struggle to generate high-quality faces that align well with textual prompts. In contrast, our MCS performs well.

cause stylized artifacts, resulting in an oil painting—like appearance, as shown in Fig. 8. In contrast, our method corrects textual prompts in advance, offering clear guidance and enabling results of more diverse and text-aligned high-quality faces. Moreover, we observe that some guided sampling-based methods, such as DDNM [33] and DPS [6], when combined with T2I models, can generate text-aligned reconstructions. As illustrated in Fig. 8, we show their results on a degraded face image. However, these methods rely on accurate knowledge of degradation processes, thus producing low-quality outputs when such priors are unavailable. In contrast, our method achieves high-quality, text-aligned face reconstruction without requiring explicit degradations.

Balance of Forward and Reverse Measurement. Our method incorporates both forward and inverse measurements, which inherently pursue conflicting goals. The forward term (\mathcal{L}_1) encourages alignment with GT, while the reverse term (\mathcal{L}_2) promotes diversity by exploring broader solution spaces. As shown in Table 5, a 1:1 weighting achieves the best trade-off between reconstruction quality and response rate. Heavier emphasis on \mathcal{L}_2 improves diversity but may lead to unrealistic facial structures, while excessive \mathcal{L}_1 suppresses diversity and limits the expressiveness of the generative prior.

Effectiveness of Selection Mechanism. In Sec. 4.1, statistical analysis shows that during steps [T, 0.6T], the T2I diffu-

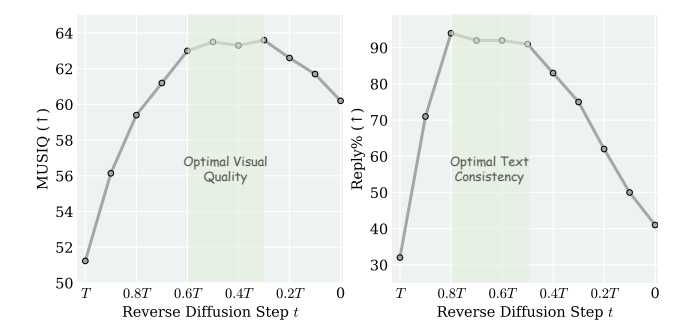


Figure 9. The boundary between forward and reverse observation at [0.6T, 0.5T] achieves the optimal balance between visual quality and diversity on $\times 8$ CelebA-HQ, demonstrating the effectiveness of the selection mechanism designed based on Fig. 4.

sion model primarily converges on structural features, while steps [0.6T,0] focus on refining details. Accordingly, the selection mechanism applies \mathcal{L}_1 gradients during [T,0.6T] and \mathcal{L}_2 gradients during [0.6T,0]. As shown in Fig. 9, we evaluated our selection mechanism based on BFR visual quality and diversity. The optimal balance is achieved when the transition between \mathcal{L}_1 and \mathcal{L}_2 gradient losses occurred in [0.6T,0.5T], further confirming the effectiveness of our selection mechanism, as supported by statistical analysis.

6. Limitation and Discussion

First, our method may struggle with fine-grained texts (e.g., subtle expressions or rare accessories), likely due to the limited granularity of text embeddings and the dominance of structural constraints. Enhancing text-vision alignment or introducing spatially grounded attention may improve it. Second, for face restoration tasks with equal input and output resolution, our method relies on an experience-based projection radius A. However, each input may possess its own optimal projection radius A. This heuristic may be suboptimal; future work could learn a degradation-aware estimator to adaptively define the projection radius.

7. Conclusion

In this paper, we propose MCS for text-prompted BFR, addressing the inherent one-to-many nature of the problem under extremely LQ real faces. Our method combines the flexibility of sampling-based approaches with the control of T2I diffusion models, enabling the generation of diverse HQ faces conditioned on textual prompts. By introducing Forward and Reverse Measurements, MCS ensures both structural alignment with inputs and semantic diversity across reconstructions. Experiments show that MCS outperforms existing BFR methods in terms of both diversity and quality, achieving prompt-aligned restoration in a training-free manner. This work advances BFR, opening new possibilities for controllable and personalized face restoration.

References

- [1] Gabriel Cardoso, Yazid Janati El Idrissi, Sylvain Le Corff, and Eric Moulines. Monte carlo guided diffusion for bayesian linear inverse problems. In *ICLR*, 2024. 1, 3, 5, 6, 7
- [2] Kelvin CK Chan, Xintao Wang, Xiangyu Xu, Jinwei Gu, and Chen Change Loy. Glean: Generative latent bank for largefactor image super-resolution. In CVPR, pages 14245–14254, 2021. 2, 6
- [3] Kelvin CK Chan, Xiangyu Xu, Xintao Wang, Jinwei Gu, and Chen Change Loy. Glean: Generative latent bank for image super-resolution and beyond. *IEEE Transactions on Pattern Analysis and Machine Intelligence*, 45(3):3154–3168, 2023.
- [4] Chaofeng Chen, Dihong Gong, Hao Wang, Zhifeng Li, and Kwan-Yee K Wong. Learning spatial attention for face superresolution. *IEEE Transactions on Image Processing*, 30:1219– 1231, 2020.
- [5] Yu Chen, Ying Tai, Xiaoming Liu, Chunhua Shen, and Jian Yang. Fsrnet: End-to-end learning face super-resolution with facial priors. In *CVPR*, pages 2492–2501, 2018. 2
- [6] Hyungjin Chung, Jeongsol Kim, Michael T Mccann, Marc L Klasky, and Jong Chul Ye. Diffusion posterior sampling for general noisy inverse problems. In *ICLR*, 2023. 1, 3, 4, 5, 6, 7, 8
- [7] Prafulla Dhariwal and Alexander Nichol. Diffusion models beat gans on image synthesis. In *NeurIPS*, pages 8780–8794, 2021. 5
- [8] Keyan Ding, Kede Ma, Shiqi Wang, and Eero P Simoncelli. Image quality assessment: Unifying structure and texture similarity. *IEEE Transactions on Pattern Analysis and Machine Intelligence*, 44(5):2567–2581, 2020. 7
- [9] Zheng Ding, Xuaner Zhang, Zhuowen Tu, and Zhihao Xia. Restoration by generation with constrained priors. In CVPR, pages 2567–2577, 2024. 6, 7
- [10] Zehao Dou and Yang Song. Diffusion posterior sampling for linear inverse problem solving: A filtering perspective. In *ICLR*, 2024. 3
- [11] Ben Fei, Zhaoyang Lyu, Liang Pan, Junzhe Zhang, Weidong Yang, Tianyue Luo, Bo Zhang, and Bo Dai. Generative diffusion prior for unified image restoration and enhancement. In *CVPR*, pages 9935–9946, 2023. 3
- [12] Kanchana Vaishnavi Gandikota and Paramanand Chandramouli. Text-guided explorable image super-resolution. In CVPR, pages 25900–25911, 2024. 3
- [13] Yuchao Gu, Xintao Wang, Liangbin Xie, Chao Dong, Gen Li, Ying Shan, and Ming-Ming Cheng. Vqfr: Blind face restoration with vector-quantized dictionary and parallel decoder. In ECCV, pages 126–143. Springer, 2022. 2, 7
- [14] Jingwen He, Wu Shi, Kai Chen, Lean Fu, and Chao Dong. Gcfsr: a generative and controllable face super resolution method without facial and gan priors. In CVPR, pages 1889– 1898, 2022. 6
- [15] Jonathan Ho, Ajay Jain, and Pieter Abbeel. Denoising diffusion probabilistic models. In *NeurIPS*, pages 6840–6851, 2020. 1, 3

- [16] Tero Karras, Timo Aila, Samuli Laine, and Jaakko Lehtinen. Progressive growing of gans for improved quality, stability, and variation. In *ICLR*, 2018. 5, 6, 7
- [17] Bahjat Kawar, Michael Elad, Stefano Ermon, and Jiaming Song. Denoising diffusion restoration models. In *NeurIPS*, pages 23593–23606, 2022. 3, 6
- [18] Junjie Ke, Qifei Wang, Yilin Wang, Peyman Milanfar, and Feng Yang. Musiq: Multi-scale image quality transformer. In *ICCV*, pages 5148–5157, 2021. 7
- [19] Bowen Li, Xiaojuan Qi, Thomas Lukasiewicz, and Philip Torr. Controllable text-to-image generation. In *NeurIPS*, 2019. 6
- [20] Wenjie Li, Mei Wang, Kai Zhang, Juncheng Li, Xiaoming Li, Yuhang Zhang, Guangwei Gao, Weihong Deng, and Chia-Wen Lin. Survey on deep face restoration: From non-blind to blind and beyond. ACM Computing Surveys, 2023. 1
- [21] Wenjie Li, Heng Guo, Xuannan Liu, Kongming Liang, Jiani Hu, Zhanyu Ma, and Jun Guo. Efficient face super-resolution via wavelet-based feature enhancement network. In ACM MM, pages 4515–4523, 2024. 2
- [22] Wenjie Li, Xiangyi Wang, Heng Guo, Guangwei Gao, and Zhanyu Ma. Self-supervised selective-guided diffusion model for old-photo face restoration. In *NeurIPS*, 2025. 1, 2, 3, 5, 6, 7
- [23] Xiaoming Li, Chaofeng Chen, Shangchen Zhou, Xianhui Lin, Wangmeng Zuo, and Lei Zhang. Blind face restoration via deep multi-scale component dictionaries. In ECCV, pages 399–415. Springer, 2020. 2
- [24] Xinqi Lin, Jingwen He, Ziyan Chen, Zhaoyang Lyu, Bo Dai, Fanghua Yu, Yu Qiao, Wanli Ouyang, and Chao Dong. Diffbir: Toward blind image restoration with generative diffusion prior. In *ECCV*, pages 430–448. Springer, 2024. 1, 2, 5, 6, 7
- [25] Robin Rombach, Andreas Blattmann, Dominik Lorenz, Patrick Esser, and Björn Ommer. High-resolution image synthesis with latent diffusion models. In CVPR, pages 10684– 10695, 2022. 2
- [26] Chitwan Saharia, William Chan, Saurabh Saxena, Lala Li, Jay Whang, Emily L Denton, Kamyar Ghasemipour, Raphael Gontijo Lopes, Burcu Karagol Ayan, Tim Salimans, et al. Photorealistic text-to-image diffusion models with deep language understanding. In *NeurIPS*, pages 36479–36494, 2022. 4, 7, 8
- [27] Jiaming Song, Arash Vahdat, Morteza Mardani, and Jan Kautz. Pseudoinverse-guided diffusion models for inverse problems. In *ICLR*, 2023. 3, 5, 6, 7, 8
- [28] Yu-Ju Tsai, Yu-Lun Liu, Lu Qi, Kelvin CK Chan, and Ming-Hsuan Yang. Dual associated encoder for face restoration. *ICLR*, 2024. 2
- [29] Xujie Wan, Wenjie Li, Guangwei Gao, Huimin Lu, Jian Yang, and Chia-Wen Lin. Attention-guided multiscale interaction network for face super-resolution. *IEEE Transactions on Systems, Man, and Cybernetics: Systems*, 2025. 2
- [30] Jianyi Wang, Zongsheng Yue, Shangchen Zhou, Kelvin CK Chan, and Chen Change Loy. Exploiting diffusion prior for real-world image super-resolution. *International Journal of Computer Vision*, pages 1–21, 2024. 2
- [31] Jingkai Wang, Jue Gong, Lin Zhang, Zheng Chen, Xing Liu, Hong Gu, Yutong Liu, Yulun Zhang, and Xiaokang Yang.

- Osdface: One-step diffusion model for face restoration. In *CVPR*, pages 12626–12636, 2025. 2, 6, 7
- [32] Xintao Wang, Yu Li, Honglun Zhang, and Ying Shan. Towards real-world blind face restoration with generative facial prior. In CVPR, pages 9168–9178, 2021. 1, 2, 5, 6, 7
- [33] Yinhuai Wang, Jiwen Yu, and Jian Zhang. Zero-shot image restoration using denoising diffusion null-space model. In *ICLR*, 2023. 1, 2, 3, 5, 6, 7, 8
- [34] Zhouxia Wang, Jiawei Zhang, Runjian Chen, Wenping Wang, and Ping Luo. Restoreformer: High-quality blind face restoration from undegraded key-value pairs. 2022. 2
- [35] Zhixin Wang, Ziying Zhang, Xiaoyun Zhang, Huangjie Zheng, Mingyuan Zhou, Ya Zhang, and Yanfeng Wang. Dr2: Diffusion-based robust degradation remover for blind face restoration. In CVPR, pages 1704–1713, 2023. 1, 2, 5, 6, 7
- [36] Rongyuan Wu, Lingchen Sun, Zhiyuan Ma, and Lei Zhang. One-step effective diffusion network for real-world image super-resolution. In *NeurIPS*, pages 92529–92553, 2024. 2
- [37] Jingwei Xin, Nannan Wang, Xinrui Jiang, Jie Li, Xinbo Gao, and Zhifeng Li. Facial attribute capsules for noise face super resolution. In *AAAI*, pages 12476–12483, 2020. 2
- [38] Peiqing Yang, Shangchen Zhou, Qingyi Tao, and Chen Change Loy. Pgdiff: Guiding diffusion models for versatile face restoration via partial guidance. In *NeurIPS*, pages 32194–32214, 2023. 1, 2, 3, 5, 6, 7
- [39] Sidi Yang, Tianhe Wu, Shuwei Shi, Shanshan Lao, Yuan Gong, Mingdeng Cao, Jiahao Wang, and Yujiu Yang. Maniqa: Multi-dimension attention network for no-reference image quality assessment. In CVPRW, pages 1191–1200, 2022. 7
- [40] Tao Yang, Peiran Ren, Xuansong Xie, and Lei Zhang. Gan prior embedded network for blind face restoration in the wild. In *CVPR*, pages 672–681, 2021. 2, 4
- [41] Zongsheng Yue and Chen Change Loy. Difface: Blind face restoration with diffused error contraction. *IEEE Transactions* on Pattern Analysis and Machine Intelligence, 2024. 1, 2, 5, 6, 7
- [42] Richard Zhang, Phillip Isola, Alexei A Efros, Eli Shechtman, and Oliver Wang. The unreasonable effectiveness of deep features as a perceptual metric. In CVPR, pages 586–595, 2018. 7
- [43] Shangchen Zhou, Kelvin Chan, Chongyi Li, and Chen Change Loy. Towards robust blind face restoration with codebook lookup transformer. In *NeurIPS*, pages 30599–30611, 2022.
- [44] Feida Zhu, Junwei Zhu, Wenqing Chu, Xinyi Zhang, Xiaozhong Ji, Chengjie Wang, and Ying Tai. Blind face restoration via integrating face shape and generative priors. In *CVPR*, pages 7662–7671, 2022. 2